nature photonics

Article

https://doi.org/10.1038/s41566-025-01750-w

Topological microwave isolator with >100-dB isolation

Received: 26 November 2024

Accepted: 28 July 2025

Published online: 16 September 2025

Check for updates

Gang Wang [1,2] & Ling Lu [1]

Microwave isolators, developed after World War II, are essential non-reciprocal devices widely used to minimize signal reflections and interference across various applications, including mobile base stations, satellite communications, radar systems, magnetic resonance imaging and industrial microwave heating. A typical commercial microwave isolator provides 20 dB of isolation, reducing the backward power by two orders of magnitude. Although higher isolation is always desired for systems that require greater power or lower noise, such as superconducting quantum computing, further reduction in the backward signal will inevitably lead to an unacceptable degradation in the forward transmission in traditional designs. Here we introduce the principle of a topological isolator, based on a unique one-way edge waveguide that spatially separates forward and backward waves, allowing for the complete absorption of the backward-propagating mode without compromising any forward signal. This ideal isolation mechanism produces an unprecedented isolation level, analytically derived to be 200 dB within a single-wavelength-size device. It is limited only by the evanescent fields within the topological bandgap in the ferrite material that spans two octaves around 10 GHz. We experimentally demonstrate this topological isolator in a stripline configuration with a minimal insertion loss of 1 dB and a backward signal deeply attenuated to the instrument noise floor. This results in an ultrahigh isolation exceeding 100 dB—an eight-orders-of-magnitude improvement over conventional counterparts. Our work not only paves the way for higher-performance isolators in the aforementioned technologies but also sets the stage for innovation in a variety of related microwave components.

An isolator[1] allows the forward signal to pass and forbids the backward signal, thereby protecting sensitive components and enhancing the overall system performance by minimizing signal reflections and cross-talk. Isolation is the key metric of isolators that quantifies their non-reciprocity, defined as the power transmission ratio between the forward and backward signals. An ideal isolator can be described by a 2×2 scattering matrix $\mathbf{S} = \begin{bmatrix} S_{11} & S_{12} \\ S_{21} & S_{22} \end{bmatrix} = \begin{bmatrix} 0 & 0 \\ 1 & 0 \end{bmatrix}$ (ref. 2), where the isolation (dB) ($20\log_{10}[|S_{21}/S_{12}|]$) is infinite. The most common isolator type—a junction isolator[3]—is illustrated in Fig. 1a; it uses a magnetized ferrite disc at its junction to split the frequencies of the counter-rotating resonator modes, inducing a typical isolation of 20 dB over a bandwidth below one octave[4,5].

However, this typical isolation level, of two orders of magnitude, is often inadequate for high-end systems with increasing power or increasing sensitivity. In quantum computing, for example, a lower bound of 60 dB is required to isolate the ambient thermal noise from the superconducting qubits at millikelvin temperatures[6]. Although

[1]Institute of Physics, Chinese Academy of Sciences/Beijing National Laboratory for Condensed Matter Physics, Beijing, China. [2]School of Physical Sciences, University of Chinese Academy of Sciences, Beijing, China. e-mail: linglu@iphy.ac.cn

https://doi.org/10.1038/s41566-025-01750-w

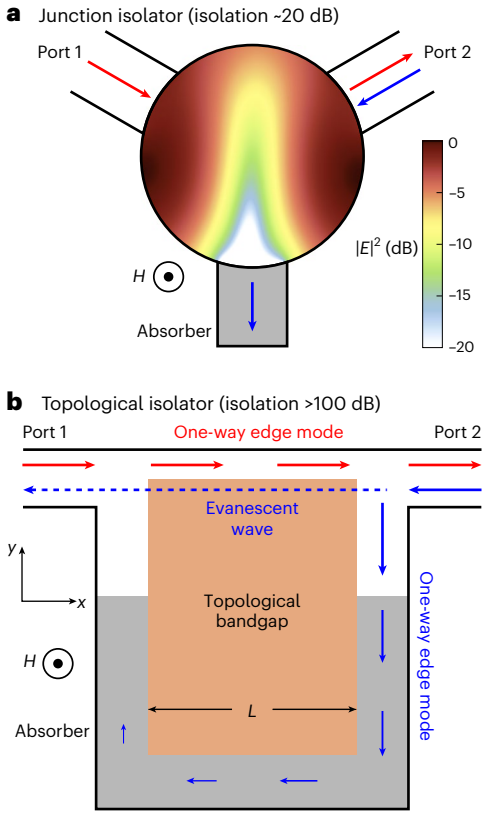

Fig. 1 | A commercial junction isolator and the proposed topological isolator. **a**, Energy distribution of a junction isolator when a signal is input at Port 1. When signal is input at Port 2, most of the energy flows into the absorber port, isolating Port 1 with around 20-dB isolation. **b**, Ultrahigh isolation of a topological isolator is determined by the evanescent wave, because the one-way backward mode can be fully absorbed.

connecting multiple isolators in series can increase isolation, this approach introduces cumulative coupling losses, a larger device footprint, potential impedance mismatches and increased complexity, all of which can degrade system performance. In addition to the junction isolator, various other types have been developed historically[7–10] and novel concepts on non-reciprocity have been proposed in recent years[11–21], but substantially improving the isolation in a compact distance remains a challenge. The general challenge is to prevent the unintended absorption of the forward signal when further absorbing the backward signal, as both forward and backward signals overlap within the same spatial region.

Principle of topological isolator

We propose to alleviate the isolation bottleneck with topological photonics[22,23]. As the most robust non-reciprocal wave phenomena discovered, the topological one-way waveguide separates the forward and backward modes spatially[24,25], enabling their independent manipulation. As depicted in Fig. 1b, the backward one-way mode can, thus, be absorbed at will by distributing the absorber along its path, without any concerns of impacting the forward signal or the reflections. Consequently, the backward-propagating mode can be attenuated to an arbitrarily low level by increasing absorption along the bottom edge of the topological isolator.

The isolation limit of the topological isolator is determined by the evanescent field that decays exponentially from the output port to the input port (Fig. 1b, blue dashed line), across the topological bandgap material. Given that the backward propagation one-way mode is entirely absorbed, the evanescent field, of the frequency inside the topological bandgap, is the sole remaining backward signal that reaches the input port. Assuming that the forward signal has perfect transmission (S_{21} = 0 dB), the limit of topological isolation is

$$\begin{aligned}\text{Isolation (dB)} &= S_{21}(\text{dB}) - S_{12}(\text{dB}) \\ &= 0 - 20\log_{10}[e^{-\beta L}] \\ &= \beta L\,(20\log_{10}[e])\end{aligned} \quad (1)$$

where β is the decay constant and L is the length of one-way waveguide between two ports. The isolation limit is only proportional to the device length (L) and the decay constant (β). L will eventually be constrained by the topological material loss to have a high-enough S_{21} and β generally increases with the width of the bandgap.

Stripline ferrite one-way edge mode

The ferrite material not only has a large topological bandgap due to the photon–magnon interaction but also a divergent β at the magnon resonance (Fig. 2a, Methods and Supplementary Section I). Ferrite has long been the material of choice for microwave isolators[26,27]; although the existence of surface states was previously known[28], their topological origin and robust nature have only been fully understood recently[29,30]. When an external magnetic field (H along the z axis) is applied perpendicular to a thin plate of ferrite whose saturation magnetization is M_s, the corresponding characteristic frequencies are the Larmor frequency of the internal magnetic field [$\omega_0 = \mu_0\gamma(H - M_s)$] and the frequency of the bias field ($\omega_H = \mu_0\gamma H$), where μ_0 and γ are the vacuum permeability and gyromagnetic ratio[2], respectively (if the ferrite is not fully magnetized [$H < M_s$], it is too lossy (Fig. 4)).

The topological bandgap opens from the magnon resonance ($\sqrt{\omega_0\omega_H}$), which is the geometric mean of the two characteristic frequencies, to the bias frequency (ω_H). In the gap, the field decay constant β diverges at the resonance frequency (the lower band edge) and vanishes at the bias frequency (the upper band edge), and so does the isolation limit according to equation (1), as verified in the simulation (Fig. 2d) in the next section. Topological one-way edge modes exist at the domain-wall interface between two ferrites of opposite magnetizations[31] (Fig. 2b). The low-frequency edge mode (Fig. 2a), dispersing from zero frequency and flattening at the Larmor resonance (ω_0), overlaps with the bulk modes in frequency. We focus on the in-gap one-way mode whose dispersion begins from zero momentum and the lower band edge, traverses the entire bandgap and converges towards the bulk dispersion at high frequencies.

We use the stripline edge-mode geometry (Fig. 2b) for a number of its advantages. First, the stripline configuration is actually a folded version of the domain wall[32], topologically equivalent but much easier to implement with one uniform magnetic field. Second, the stripline edge is defined by the edge of the central conductor, rather than the ferrite edge, which is more lossy than the bulk due to the extra surface disruption. Third, the stripline configuration is the standard geometry for commercial isolators[33], featuring a central conductor sandwiched between two ferrite plates sealed with parallel ground planes. Historically, isolators utilizing a similar edge structure are referred to as the edge-guided mode isolator[10]. However, neither the topological protection of the edge mode nor the underlying principle of topological isolation was recognized at the time. Despite extensive research on this device[34–37], the overall performance of edge-guided mode isolators remains inferior to that of junction isolators.

Design of topological isolator

Our design of the topological ferrite isolator is shown in Fig. 2c, based on the one-way stripline edge mode. Similar to a commercial stripline device, the topological isolator consists of four materials: ferrite, copper, absorber and aluminium. The dimensions of the two ferrite plates are 25 mm (L) × 50.8 mm × 0.4 mm. The copper film with 0.2-mm

https://doi.org/10.1038/s41566-025-01750-w

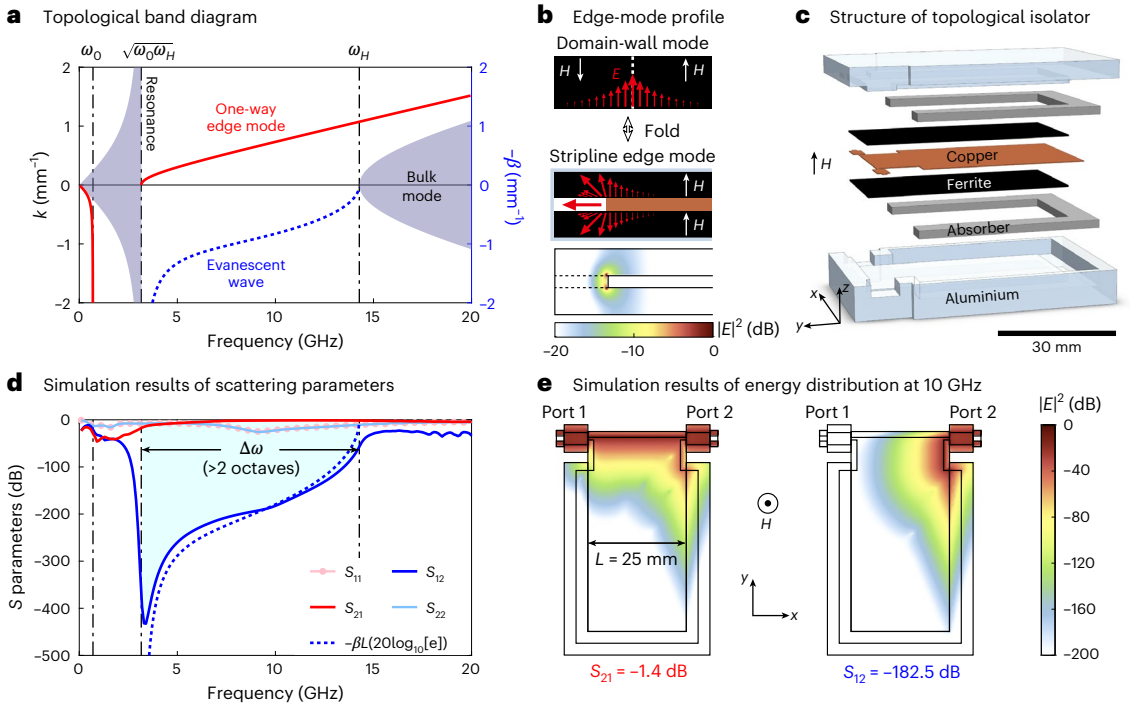

Fig. 2 | Design of the topological isolator. a, Band structure of the ferrite one-way edge mode. **b**, Mode profile of the stripline edge mode and its topological equivalence to the ferrite domain-wall mode. **c**, Exploded view of the stripline ferrite topological isolator. **d**, Calculated scattering parameters of the topological isolator. **e**, Simulated energy distributions at 10 GHz, when the signal is input from Port 1 (left) and from Port 2 (right).

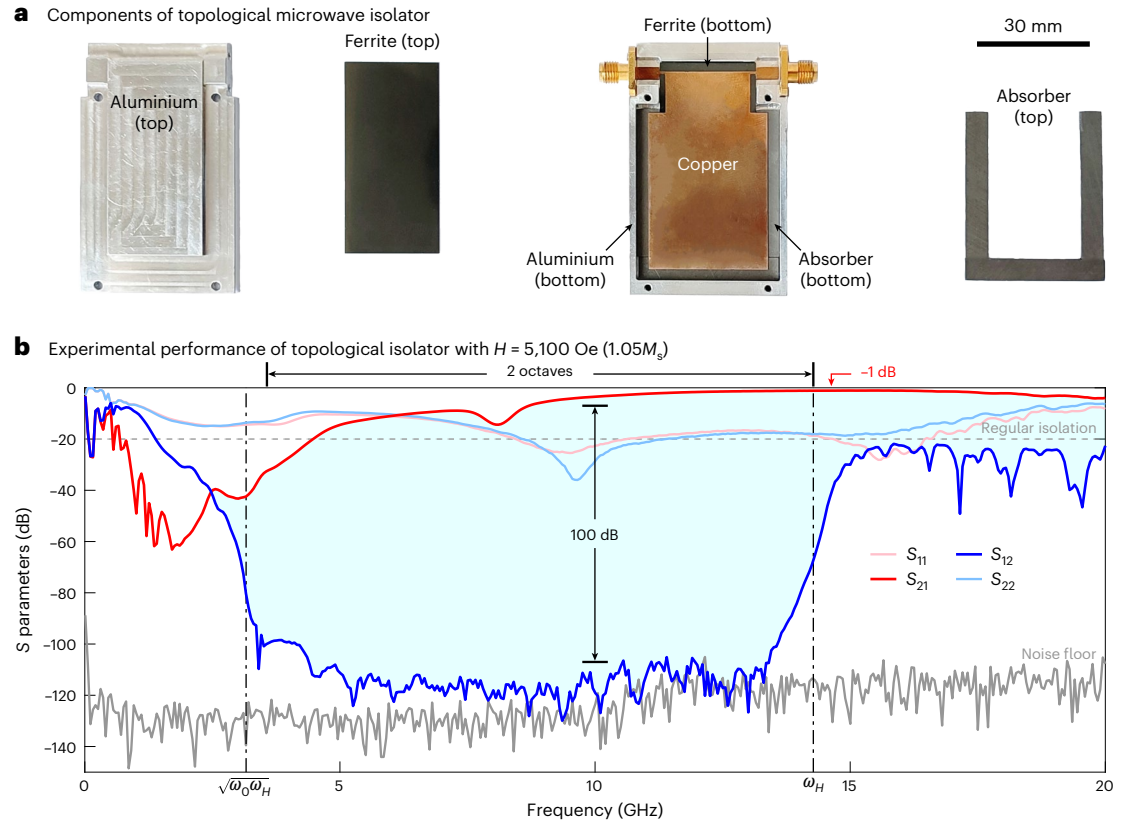

Fig. 3 | Experimental performance of the topological isolator. a, Disassembled view of the isolator showing all components laid out. **b**, Experimental scattering parameters of the device (M_s = 4,850 Oe), showing isolation greater than 100 dB. The two dash–dotted vertical lines represent the edges of the topological bandgap.

https://doi.org/10.1038/s41566-025-01750-w

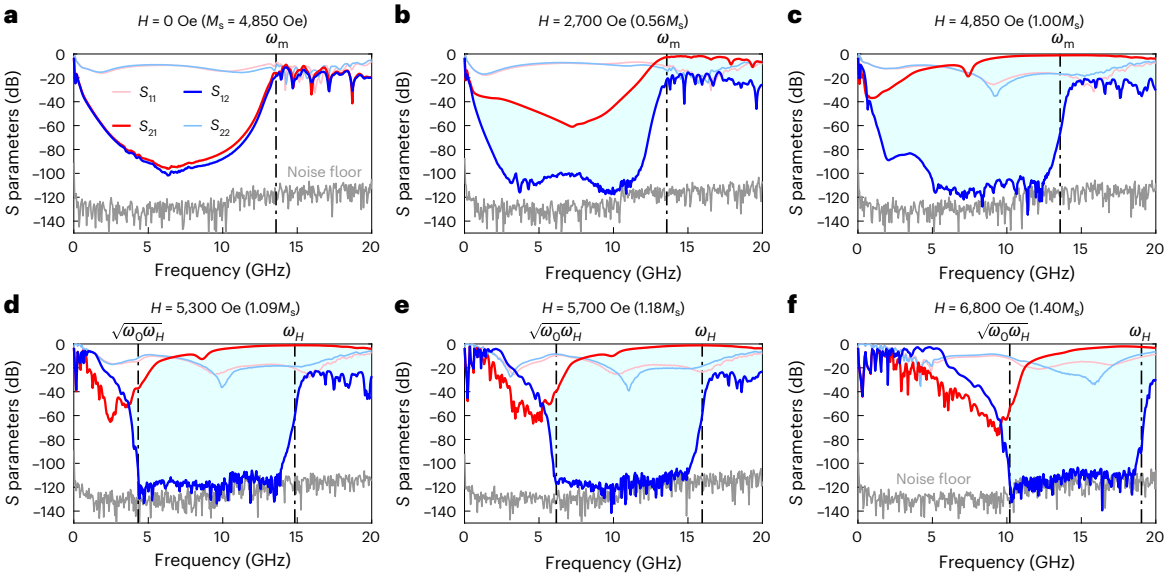

Fig. 4 | Topological isolator under varying *H* values. a–**f**, Scattering parameters of the topological isolator when *H* sweeps across the ferrite's M_s.

thickness is the central conductor of the stripline. The top copper geometry near the ports (Figs. 2c,e and 3a) is engineered to impedance-match the edge mode for higher S_{21}. The bottom copper geometry is widened into the absorber for lower S_{12}. Silicone absorbers are placed on the sides of the ferrites with a thickness of 1.2 mm. The aluminium provides metallic boundaries to support and seal the entire device.

The simulated scattering parameters of the topological isolator are plotted in Fig. 2d (detailed in Methods). To reveal the isolation limits determined by the evanescent fields, we set the absorption coefficient of the absorber to be sufficiently large (Supplementary Section II) such that S_{12} no longer changes. The results show an extremely large isolation level inside the topological bandgap with a bandwidth of over two octaves. The isolation is 60 dB at the upper band edge, reaches 200 dB at the mid-gap and exceeds 400 dB around the lower band edge. Although the isolation is divergently high at the magnon resonance, it is not a proper device operation point due to the strong material absorption and a resulting low forward transmission ($S_{21} \approx -18$ dB). Comparing Fig. 2a,d, it is evident that this isolation limit is governed by equation (1).

The unprecedented topological isolation is consistent with the field profiles inside the isolator. The energy distributions at 10 GHz are presented in Fig. 2e. The left panel displays the energy distribution of the forward signal from Port 1, with a small insertion loss $S_{21} = -1.4$ dB. The right panel displays the energy absorption of the backward signal from Port 2, confirming that only the evanescent field reaches Port 1. This isolation of $S_{21} - S_{12} \approx 181$ dB is an extremely high number for a single-wavelength-size device, indicating a substantial potential advantage over conventional isolators. The field profiles at 3.5 GHz and of a more compact device are plotted in Extended Data Fig. 1.

Experimental results

Encouraged by the theoretical results, we fabricate the topological isolator, with its components displayed in Fig. 3a. A magnetic field of $H = 5{,}100$ Oersted (Oe) is applied, slightly exceeding the ferrite's saturation magnetization and consistent with the theoretical setting shown in Fig. 2. The key characteristics of the experimental results presented in Fig. 3b closely align with those in Fig. 2d.

The experimental isolation exceeds 100 dB (Fig. 3b), equivalent to at least five commercial isolators connected in series (as compared directly in Extended Data Fig. 2). Moreover, this ultrahigh isolation level is still substantially lower than the predicted limit of 200 dB (Fig. 2d). This is because the absorption of the backward mode is complete in simulation but incomplete in experiment, due to the limited absorption coefficient of the absorber in use (Supplementary Section II). Although extending the backward path could easily enhance isolation (Supplementary Section III), the current device footprint is limited by the size of the magnet (Methods and Supplementary Section IV). More critically, the current return signal (S_{12}) already approaches the instrument noise floor of around −120 dB (Fig. 3b, grey line), preventing the characterization of higher isolation levels.

The ultrahigh isolation occurs within the predicted topological bandgap, which spans over two octaves from 3 GHz to 14 GHz. Beyond the bandgap, the isolation drops to around 20 dB and remains consistent up to 43 GHz (Extended Data Fig. 3a). This over-three-octave isolation effect (from 3 GHz to 43 GHz) results from the ultrawideband one-way edge dispersion, experimentally confirmed in Extended Data Fig. 3b. The reduced isolation level of 20 dB above 14 GHz, same level as that of commercial isolators, is attributed to the coexistence of two-way bulk states beyond the bandgap. This further emphasizes that without completely eliminating the backward modes using one-way waveguides, it is challenging to increase isolation much above 20 dB.

The peak experimental transmission of $S_{21} = -1$ dB (80%) occurs near the upper band edge of the topological bandgap, closely matching the simulation results shown in Fig. 2d. At lower frequencies, the experimental S_{21} is a few decibels lower than the simulation results. This discrepancy arises because the material model (Methods) used in the simulation assumes that the ferrite is completely magnetized. In practice, however, not all magnetic dipoles align with the external field due to lattice imperfections, magnetic interactions and boundary terminations in ferrites. This leads to reduced magnetization and increased ferrite loss[38], particularly near the magnon resonance where the absorption peaks (Supplementary Section V).

A transmission dip in S_{21} (Fig. 3b) is observed inside the bandgap that does not appear in the simulation results shown in Fig. 2d. This dip arises from the surface effect of the ferrite, where the surface saturation magnetization is lower than that of the bulk. Consequently, the surface Larmor frequency shifts into the bulk bandgap (Fig. 2a) and the corresponding slow-light edge mode enhances absorption. In Extended Data Fig. 4, we model this surface effect and reproduce the experimental dip in simulation. More details are provided in Extended Data Fig. 5 and Supplementary Section VI.

Bias tuning

We present the evolution of the scattering parameters of the topological isolator under varying external bias fields (Fig. 4) by adjusting the current in the electromagnet. Without the bias field (Fig. 4a), the ferrite behaves as a reciprocal and lossy medium, resulting in equally low transmissions for both S_{21} and S_{12} below the magnetization frequency ($\omega_m = \mu_0 \gamma M_s = \omega_H - \omega_0$). When an external bias is applied (Fig. 4b), S_{21} rises as the ferrite loss decreases[38]. Simultaneously, the backward signal (S_{12}) continues to drop due to the formation of the backward one-way mode at the edge, where the modal energy overlaps the absorber and dissipates more rapidly. As the external bias reaches (Fig. 4c) or just exceeds (Fig. 3b) M_s of the ferrite, both S_{21} and isolation bandwidth reach their maximum values. Further increases in external bias beyond M_s (Fig. 4d–f) shift the bandgap to higher frequencies, demonstrating wavelength tunability. At these high biases ($H > M_s$), S_{12} in the bandgap is consistently below −100 dB and fluctuates near the noise floor of the instrument.

Conclusion

We introduce the concept, explain the principle, design the model, construct the prototype and test the performance of a topological isolator that achieves an isolation greater than 100 dB with a ferrite length of less than one vacuum wavelength. Despite the ultrahigh level, the achieved isolation still falls short of the predicted theoretical limit by ten orders of magnitude (Fig. 2d), leaving considerable room for future improvement. For example, a more advanced absorption technique could further increase isolation or shrink the device footprint, by using a more efficient absorber or a slower backward one-way mode[39,40]. In addition, optimizing the coupling design—from SubMiniature version A connector (SMA) to the edge mode—could improve the broadband transmission or reduce the coupling length. Our findings demonstrate the potential of topological photonics[41–43] to drive innovation in microwave technologies[2], a field ubiquitously used but often considered mature.

Online content

Any methods, additional references, Nature Portfolio reporting summaries, source data, extended data, supplementary information, acknowledgements, peer review information; details of author contributions and competing interests; and statements of data and code availability are available at https://doi.org/10.1038/s41566-025-01750-w.

References

1. Button, K. Microwave ferrite devices: the first ten years. *IEEE Trans. Microw. Theory Techn.* **32**, 1088–1096 (1984).
2. Pozar, D. M. *Microwave Engineering* 4th edn (John Wiley & Sons, 2012).
3. Linkhart, D. K. *Microwave Circulator Design* 2nd edn (Artech House, 2014).
4. Bosma, H. On stripline Y-circulation at UHF. *IEEE Trans. Microw. Theory Techn.* **12**, 61–72 (1964).
5. Fay, C. & Comstock, R. Operation of the ferrite junction circulator. *IEEE Trans. Microw. Theory Techn.* **13**, 15–27 (1965).
6. Krinner, S. et al. Engineering cryogenic setups for 100-qubit scale superconducting circuit systems. *EPJ Quantum Technol* **6**, 2 (2019).
7. Enander, B. A new ferrite isolator. *Proc. IRE* **44**, 1421–1430 (1956).
8. Weisbaum, S. & Seidel, H. The field displacement isolator. *Bell Syst. Tech. J.* **35**, 877–898 (1956).
9. Schlomann, E. On the theory of the ferrite resonance isolator. *IRE Trans. Microw. Theory Techn.* **8**, 199–206 (1960).
10. Hines, M. Reciprocal and nonreciprocal modes of propagation in ferrite stripline and microstrip devices. *IEEE Trans. Microw. Theory Techn.* **19**, 442–451 (1971).
11. Jalas, D. et al. What is—and what is not—an optical isolator. *Nat. Photon.* **7**, 579–582 (2013).
12. Estep, N. A., Sounas, D. L., Soric, J. & Alù, A. Magnetic-free non-reciprocity and isolation based on parametrically modulated coupled-resonator loops. *Nat. Phys.* **10**, 923–927 (2014).
13. Shi, Y., Yu, Z. & Fan, S. Limitations of nonlinear optical isolators due to dynamic reciprocity. *Nat. Photon.* **9**, 388–392 (2015).
14. Sounas, D. L., Soric, J. & Alù, A. Broadband passive isolators based on coupled nonlinear resonances. *Nat. Electron.* **1**, 113–119 (2018).
15. Kord, A., Sounas, D. L. & Alu, A. Microwave nonreciprocity. *Proc. IEEE* **108**, 1728–1758 (2020).
16. Nagulu, A. & Krishnaswamy, H. Non-magnetic non-reciprocal microwave components—state of the art and future directions. *IEEE J. Microw.* **1**, 447–456 (2021).
17. Zhang, Z., Delplace, P. & Fleury, R. Superior robustness of anomalous non-reciprocal topological edge states. *Nature* **598**, 293–297 (2021).
18. Fernandes, D. E., Pereira, R. A., Lannebère, S., Morgado, T. A. & Silveirinha, M. G. Experimental verification of ill-defined topologies and energy sinks in electromagnetic continua. *Adv. Photon.* **4**, 035003 (2022).
19. Masui, S., Kojima, T., Uzawa, Y. & Onishi, T. A novel microwave nonreciprocal isolator based on frequency mixers. *IEEE Microw. Wireless Technol. Lett.* **33**, 1051 (2023).
20. Jiang, T. et al. Wideband isolator based on one-way surface magnetoplasmons with ultra-high isolation. *Sci. Rep.* **14**, 17474 (2024).
21. Jia, R. et al. On-chip active non-reciprocal topological photonics. *Adv. Mater.* **37**, 2501711 (2025).
22. Lu, L., Joannopoulos, J. D. & Soljačić, M. Topological photonics. *Nat. Photon.* **8**, 821–829 (2014).
23. Ozawa, T. et al. Topological photonics. *Rev. Mod. Phys.* **91**, 015006 (2019).
24. Haldane, F. D. M. & Raghu, S. Possible realization of directional optical waveguides in photonic crystals with broken time-reversal symmetry. *Phys. Rev. Lett.* **100**, 013904 (2008).
25. Wang, Z., Chong, Y., Joannopoulos, J. D. & Soljačić, M. Observation of unidirectional backscattering-immune topological electromagnetic states. *Nature* **461**, 772–775 (2009).
26. Fuller, A. J. B. *Ferrites at Microwave Frequencies* (IET, 1987).
27. Harris, V. G. Modern microwave ferrites. *IEEE Trans. Magn.* **48**, 1075–1104 (2012).
28. Hartstein, A., Burstein, E., Maradudin, A. A., Brewer, R. & Wallis, R. F. Surface polaritons on semi-infinite gyromagnetic media. *J. Phys. C: Solid State Phys.* **6**, 1266 (1973).
29. Silveirinha, M. G. Chern invariants for continuous media. *Phys. Rev. B* **92**, 125153 (2015).
30. Okamoto, A., Shindou, R. & Murakami, S. Berry curvature for coupled waves of magnons and electromagnetic waves. *Phys. Rev. B* **102**, 064419 (2020).
31. Zhang, X., Li, W. & Jiang, X. Confined one-way mode at magnetic domain wall for broadband high-efficiency one-way waveguide, splitter and bender. *Appl. Phys. Lett.* **100**, 041108 (2012).
32. Seewald, C. K. & Bray, J. R. Ferrite-filled antisymmetrically biased rectangular waveguide isolator using magnetostatic surface wave modes. *IEEE Trans. Microw. Theory Techn.* **58**, 1493–1501 (2010).
33. Helszajn, J. *The Stripline Circulator: Theory and Practice* (John Wiley & Sons, 2008).
34. Courtois, L., Bernard, N., Chiron, B. & Forterre, G. A new edge-mode isolator in the very high frequency range. *IEEE Trans. Microw. Theory Techn.* **24**, 129–135 (1976).
35. Talisa, S. & Bolle, D. On the modeling of the edge-guided mode stripline isolators. *IEEE Trans. Microw. Theory Techn.* **27**, 584–591 (1979).

36. Fesharaki, F., Akyel, C. & Wu, K. Broadband substrate integrated waveguide edge-guided mode isolator. *Electron. Lett.* **49**, 269–271 (2013).
37. Zeng, L., Tong, C.-Y. E. & Paine, S. N. A low-insertion loss cryogenic edge-mode isolator with 18 GHz bandwidth. *IEEE J. Microw.* **3**, 1258–1266 (2023).
38. Green, J. & Sandy, F. Microwave characterization of partially magnetized ferrites. *IEEE Trans. Microw. Theory Techn.* **22**, 641–645 (1974).
39. Guglielmon, J. & Rechtsman, M. C. Broadband topological slow light through higher momentum-space winding. *Phys. Rev. Lett.* **122**, 153904 (2019).
40. Chen, F. et al. Multiple Brillouin zone winding of topological chiral edge states for slow light applications. *Phys. Rev. Lett.* **132**, 156602 (2024).
41. Qiu, W., Wang, Z. & Soljačić, M. Broadband circulators based on directional coupling of one-way waveguides. *Opt. Express* **19**, 22248 (2011).
42. Cheng, X. et al. Robust reconfigurable electromagnetic pathways within a photonic topological insulator. *Nat. Mater.* **15**, 542–548 (2016).
43. Ma, S. & Anlage, S. M. Microwave applications of photonic topological insulators. *Appl. Phys. Lett.* **116**, 250502 (2020).

Methods

Ferrite model

Ferrites are ferrimagnetic materials widely used in commercial isolators, and they are characterized by their M_s values. When the ferrite is fully magnetized under an external magnetic field ($H > M_s$) applied along the z direction, its permeability tensor ($\boldsymbol{\mu}$) has the following gyrotropic form[2]:

$$\boldsymbol{\mu} = \begin{bmatrix} \mu & \mathrm{j}\kappa & 0 \\ -\mathrm{j}\kappa & \mu & 0 \\ 0 & 0 & \mu_0 \end{bmatrix}, \tag{2}$$

where $\mu = \mu_0 \frac{\omega_0\omega_H - \omega^2}{\omega_0^2 - \omega^2}$ and $\kappa = \mu_0 \frac{\omega\omega_m}{\omega_0^2 - \omega^2}$. The internal magnetic field is given by $H_0 = H - M_s$ for a thin ferrite plate in the x–y plane. The Larmor frequency is $\omega_0 = \mu_0\gamma H_0$, the bias frequency is $\omega_H = \mu_0\gamma H$, and the magnetization frequency is $\omega_m = \mu_0\gamma M_s$.

The bulk bandgap opens for the extraordinary wave (Fig. 2a and Supplementary Section I), whose wavevector propagates in the x–y plane and the electric field aligns with H along the z axis. The bandgap frequency, determined by the bulk dispersion relation $k^2 = \omega^2\epsilon\mu_{\mathrm{eff}} = \omega^2\epsilon\mu_0 \frac{\omega_H^2 - \omega^2}{\omega_0\omega_H - \omega^2}$ (ref. 2), ranges from $\sqrt{\omega_0\omega_H}$ (resonance frequency) to ω_H (bias frequency), between which the wavevector is imaginary ($k^2 = -\beta^2 < 0$), where β is the field decay constant. The larger the M_s, the larger the gap. The edge-mode dispersions of $k^2 = \omega^2\epsilon\mu = \omega^2\epsilon\mu_0 \frac{\omega_0\omega_H - \omega^2}{\omega_0^2 - \omega^2}$ (ref. 31) are plotted in Fig. 2a (two red lines) and derived in Supplementary Section I.

If the microwave magnetic loss of the ferrite is considered, we replace ω_0 and ω_H with $\omega_0 + \mathrm{j}\frac{\mu_0\gamma\Delta H}{2}$ and $\omega_H + \mathrm{j}\frac{\mu_0\gamma\Delta H}{2}$ respectively, where ΔH is the linewidth of the Larmor resonance[2]. For the nickel spinel ferrite, we use $\Delta H = 80$ Oe. The frequency-dependent parameters $\mu = \mu' - \mathrm{j}\mu''$, $\kappa = \kappa' - \mathrm{j}\kappa''$ and $\mu_{\mathrm{eff}} = \mu'_{\mathrm{eff}} - \mathrm{j}\mu''_{\mathrm{eff}}$ are plotted in Extended Data Fig. 6. The dielectric constant of ferrite is $\epsilon = \epsilon' - \mathrm{j}\epsilon'' = \epsilon' - \mathrm{j}\epsilon'\tan\delta$, where $\tan\delta$ is the dielectric loss tangent of ferrite. For the nickel spinel ferrite, we use $\epsilon' = 13.5$ and $\tan\delta = 0.0002$. Such a small dielectric loss can be ignored in simulations.

Simulation

We use COMSOL Multiphysics 5.4 to simulate the scattering parameters and field profiles of the topological isolator, in which the SMA ports are modelled by the 'coaxial ports' for frequency scans. A number of measures are used to reduce the computational time and complexity. First, copper and aluminium are approximated as perfect electrical conductors. Second, due to the up-down mirror symmetry of the stripline, half of the structure is simulated. Third, only the odd mode is considered, by using a perfect-magnetic-conductor boundary at the middle copper plane, to compute the fundamental transverse electromagnetic mode of the stripline.

Fabrication and measurement

We choose nickel spinel ferrites for its large saturation magnetization ($M_s = 4{,}850$ Oe), resulting in a large bandgap and isolation. The material parameters and losses of the ferrite are tabulated in Supplementary Section II. Beryllium copper is used as the central conductor, due to its high strength and high conductivity, whose shape is defined by wet etching. We use the Eccosorb BSR/MFS absorber thicker than 1 mm for sufficient absorption.

The electromagnet (Supplementary Section IV) supplies an external uniform magnetic field in an area of 50 mm × 50 mm from 0 Oe to 10,000 Oe by adjusting the currents. The experimental scattering parameters in the main text are collected using a vector network analyser (Keysight N5230A, 10 MHz to 20 GHz), calibrated by a calibration module (Keysight N4691B). The scattering parameters shown in Extended Data Fig. 3 are collected using another vector network analyser (Keysight N5224B, 10 MHz to 43.5 GHz), calibrated by a calibration module (Keysight N4693D). The instrument noise floor is the transmittance when the vector network analyser ports are sealed.

Data availability

The data presented in the main text are available via Figshare at https://doi.org/10.6084/m9.figshare.29554457 (ref. 44). All other data that support the findings of this work are available from the corresponding author on reasonable request.

References

44. Wang, G. SourceData.zip. *Figshare* https://doi.org/10.6084/m9.figshare.29554457 (2025).

Acknowledgements

We thank Q. Yan, X. Zhao, R. Liu, W. Sun, T. Zheng and Z. Li for discussions. This work was supported by the Natural Science Foundation of China (12025409), by the Chinese Academy of Sciences through the Project for Young Scientists in Basic Research (YSBR-021) and through the IOP-HKUST-Joint Laboratory for Wave Functional Materials Research, and by the Beijing Natural Science Foundation (Z200008).

Author contributions

G.W. performed the design, simulations, experiments and wrote the paper with L.L., who initiated and supervised the project.

Competing interests

The authors declare no competing interests.

Additional information

Extended data is available for this paper at https://doi.org/10.1038/s41566-025-01750-w.

Supplementary information The online version contains supplementary material available at https://doi.org/10.1038/s41566-025-01750-w.

Correspondence and requests for materials should be addressed to Ling Lu.

Peer review information *Nature Photonics* thanks the anonymous reviewers for their contribution to the peer review of this work.

https://doi.org/10.1038/s41566-025-01750-w

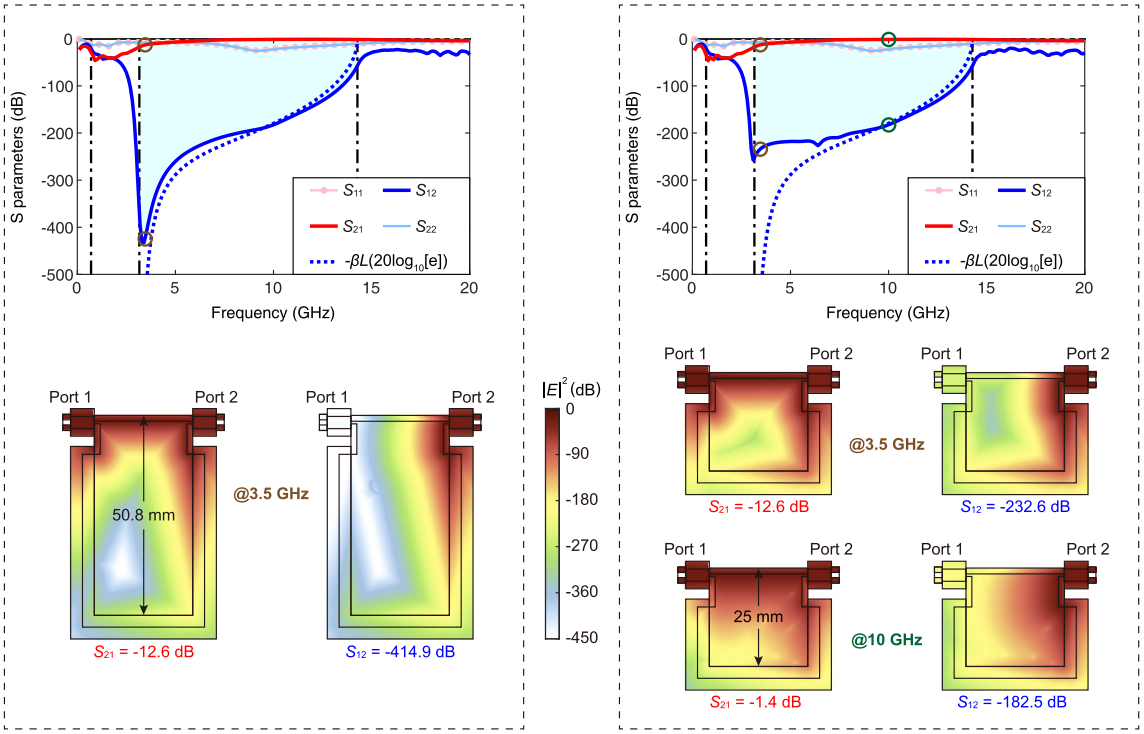

Extended Data Fig. 1 | Simulation results of topological isolators with different sizes in y-direction. The left panel presents the scattering parameters of a device with a ferrite length of 50.8 mm, identical to Fig. 2d, along with the corresponding energy distributions at 3.5 GHz. The right panel presents the scattering parameters of a device with a ferrite length of 25 mm, along with the energy distributions at 3.5 GHz and 10 GHz. The absorber used in these simulations is the same as that in Fig. 2d,e, as listed in Supplementary Table S1.

https://doi.org/10.1038/s41566-025-01750-w

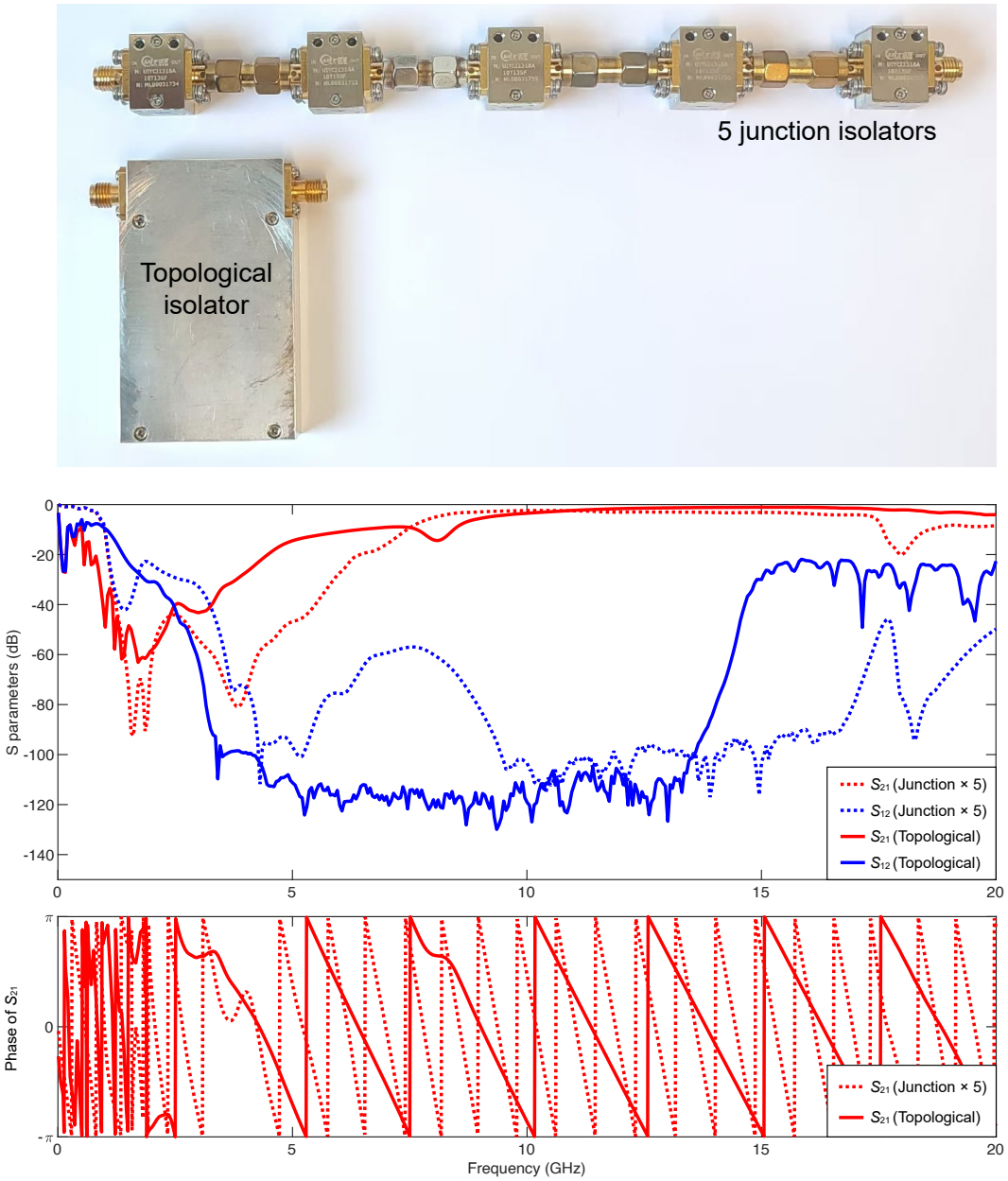

Extended Data Fig. 2 | Comparison between 1 topological isolator and 5 junction isolators (UIYCI1318A10T13SF) connected in series. Note that, even in this case, our topological isolator could have higher transmission, higher isolation, and lower group delay. The group delay time of the forward signal in the device is $t = \frac{d\varphi}{d\omega}$, where φ represents the phase of S_{21} and ω is the angular frequency. Consequently, a single topological isolator exhibits about 1/3 group delay compared to 5 junction isolators.

https://doi.org/10.1038/s41566-025-01750-w

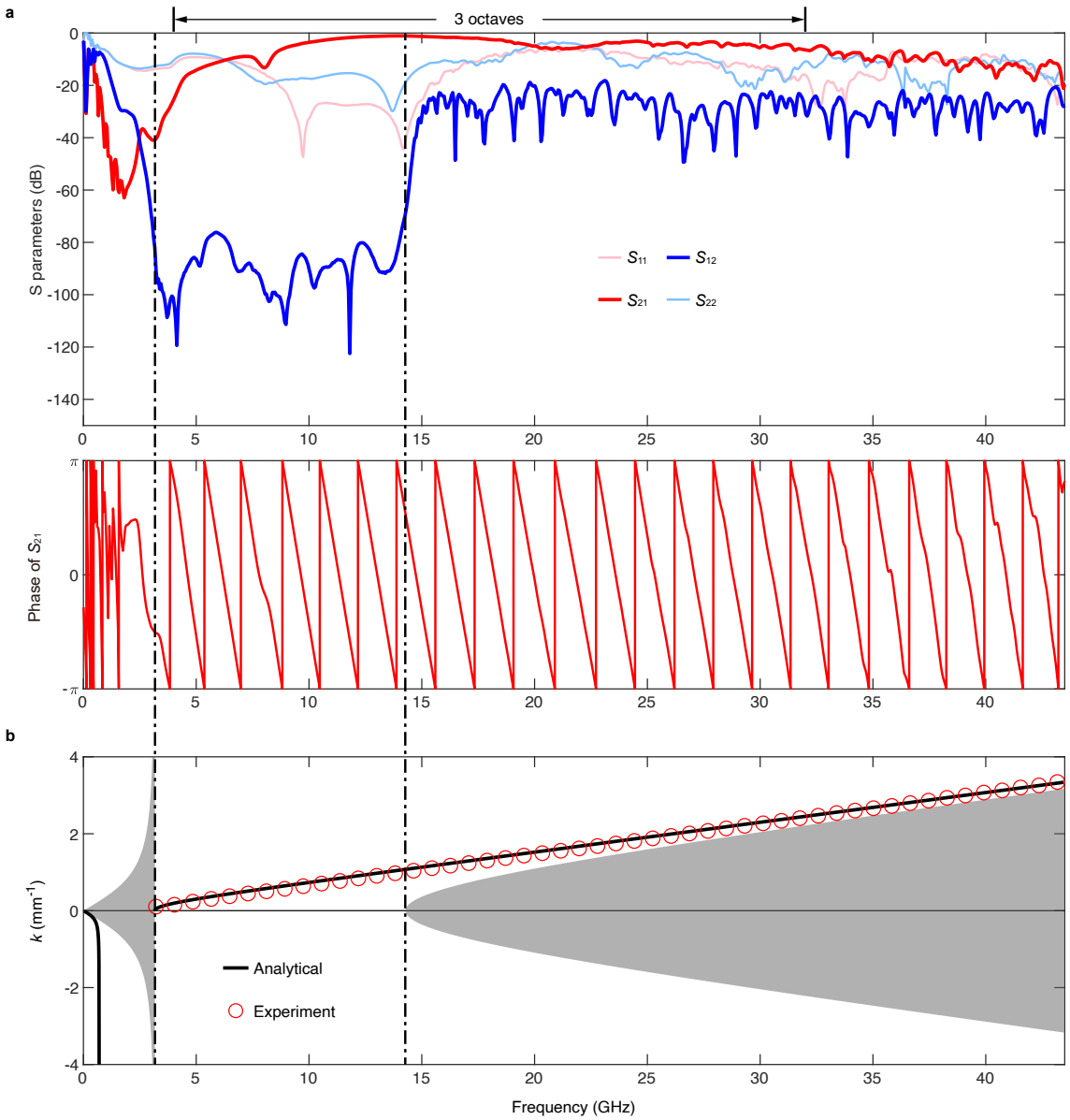

Extended Data Fig. 3 | Ultrawideband response (up to 43.5 GHz) of the topological microwave isolator. a. Experimental scattering parameters with the phase of S_{21}. **b.** Propagation constants of stripline one-way edge mode extracted from experimental data using (Phase of S_{21})/(Propagation distance of S_{21}), which fit well with the analytical results.

https://doi.org/10.1038/s41566-025-01750-w

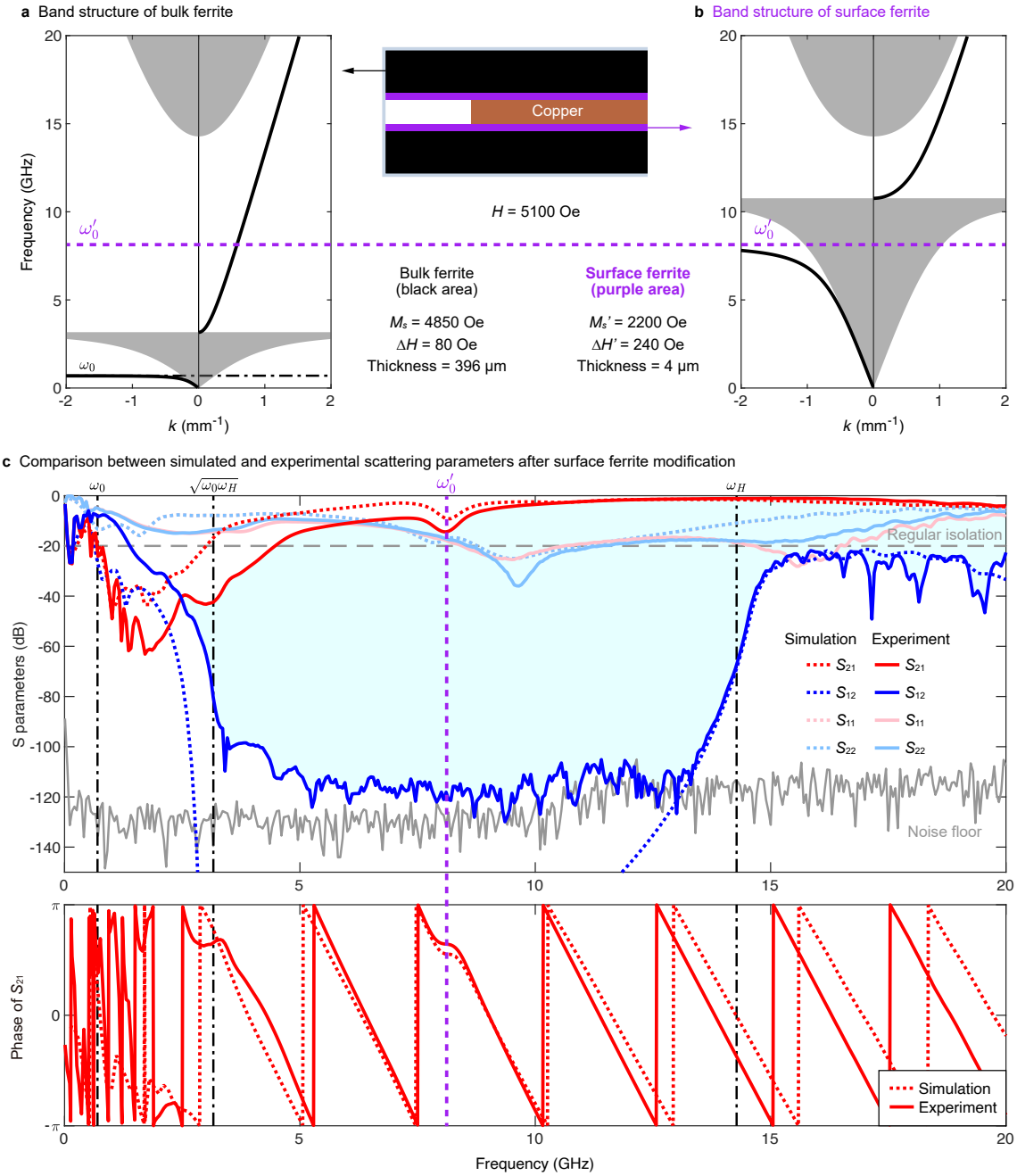

Extended Data Fig. 4 | S_{21} dip due to surface effect of ferrite. a. Photonic band structure of bulk ferrite. **b**. Photonic band structure of surface ferrite. **c**. Comparison between simulated and experimental scattering parameters after surface ferrite modification. The saturation magnetization of the surface layer is determined by the dip frequency, which equals the Larmor frequency (ω_0') of the surface ferrite, being higher than the bulk Larmor frequency (ω_0). The Larmor resonance linewidth ($\Delta H'$) of the surface layer is determined by the spectral width of the transmission dip. The thickness of the surface layer is determined by the depth of the S_{21} dip. The details of the modeling are in Supplementary Section VI.

https://doi.org/10.1038/s41566-025-01750-w

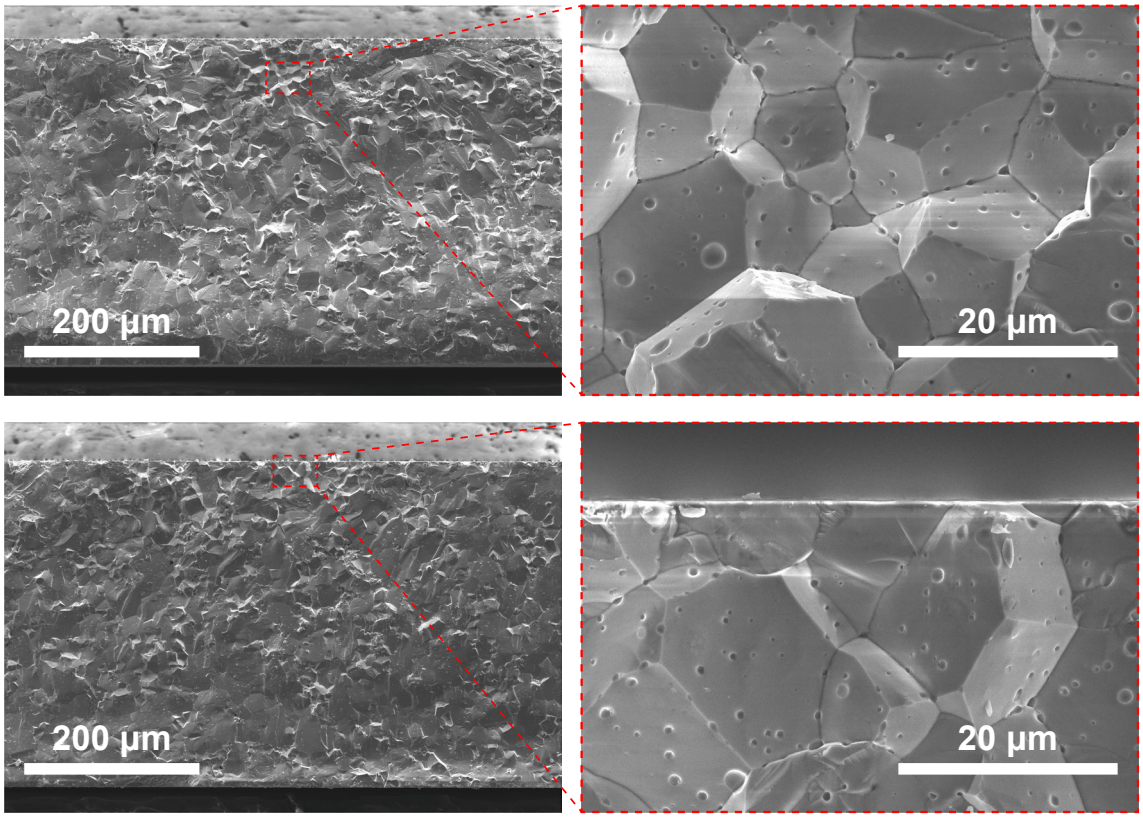

Extended Data Fig. 5 | SEM images of the sidewall cross-section of the 400 µm-thick nickel spinel ferrite used in the topological isolator, exhibiting micron-scale grain sizes.

https://doi.org/10.1038/s41566-025-01750-w

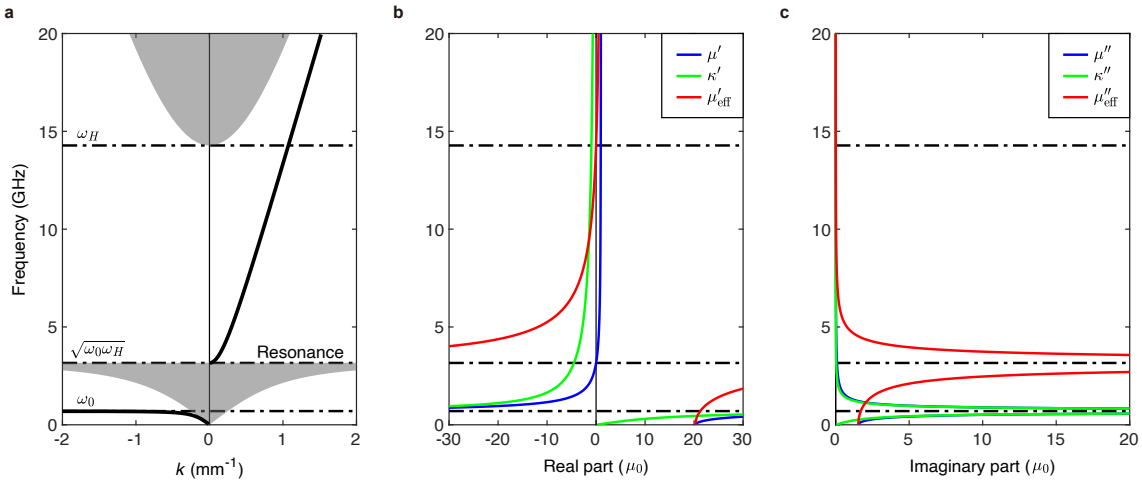

Extended Data Fig. 6 | Permeability parameters of nickel spinel ferrite, when H = 5,100 Oe, M_s = 4,850 Oe, and ΔH = 80 Oe. a. Band structure of nickel spinel ferrite. **b**. Real part of permeability. **c**. Imaginary part of permeability.